Atmospheric Research 270 (2022) 106079

Contents lists available at ScienceDirect

Atmospheric Research

journal homepage: www.elsevier.com/locate/atmosres

Decomposition of water vapor flux divergence and its application to a blizzard event over Ili Valley in Central Asia during 30 Nov to 1 Dec 2018

Shuping Ma [a,b,c,1], Jie Cao [a,b,d,1,*], Haijun Zhao [e,f], Xuan Zhou [g], Lingkun Ran [b,c]

[a] *Key Laboratory of Meteorological Disaster (KLME), Ministry of Education & Collaborative Innovation Center on Forecast and Evaluation of Meteorological Disasters (CIC-FEMD), Nanjing University of Information Science & Technology, Nanjing 210044, China*
[b] *University of Chinese Academy of Sciences, Beijing 100049, China*
[c] *Institute of Atmospheric Physics, Chinese Academy of Sciences, Beijing 100029, China*
[d] *Cooperative Institute for Mesoscale Meteorological Studies (CIMMS), University of Oklahoma, Norman 73072, USA*
[e] *Xinjiang Uygur Autonomous Region Meteorological Service, Urumqi 830002, China*
[f] *Shandong Key Laboratory of Meteorological Disaster prevention and reduction, Jinan 250031, China*
[g] *Beijing Weather Forecast Center, Beijing 100089, China*

ARTICLE INFO

Keywords:
Extreme precipitation
Central Asia
Flow decomposition
Water vapor flux divergence
Complex terrain

ABSTRACT

Central Asia is experiencing an increase in the occurrence of extreme flood events while still featuring in scarce precipitation. These extreme events are governed by weather systems of various scales as well as complex terrain effects. It is therefore difficult to analyze and forecast precipitation with traditional methods. In this study, an approach is designed by decomposing water vapor flux divergence (Q_v^{all}) under model's terrain following coordinates following the Helmholtz theorem. The traditionally used but important variable for depicting anomalous precipitation, Q_v^{all}, is partitioned into three components, *i.e.*, flow divergence (Q_v^{div}), moisture advections by large-scale motion (Q_v^{L}) and by sub-synoptic motion (Q_v^{S}). Applications to a blizzard event occurred over Ili Valley during 30 Nov to 1 Dec 2018 is performed as an example. The eastward water vapor flux brings moisture from Balkhash Lake to Ili Valley during the entire precipitation event, while Q_v^{all} fails to indicate the initiation and weakening of precipitation. Temporal and spatial evolutions of the three decomposed components are analyzed with comparison to precipitation on both windward slope and lee side. Q_v^{div} with dominant magnitude always converges no matter precipitation intensifies or weakens, and therefore leads to false moisture aggregation signals in Q_v^{all}. The other two components, Q_v^{L} and Q_v^{S}, converge prior to precipitation and diverge or weaken before the event ends. Besides, Q_v^{L} performs better than Q_v^{S} on windward slope and shows moisture transport from upper levels while Q_v^{S} achieves better on lee side. Future applications of this flow decomposition approach may thus extend to improving precipitation predictions with negligible computational costs over complex topography in other places around the world.

1. Introduction

Featuring in scarce precipitation, Central Asia (CA) is one of the largest drylands which suffers tremendous social and economic losses from severe droughts (Schiemann et al., 2008). Upstream of China, weather and climate in CA have critical impact on regional climate change. Sensitive to global climate change, precipitation in CA responds in the form of increasing trend in the occurrence of extreme events (Bothe et al., 2012; Duan et al., 2015). In the past 10 years, local rainstorms account for 36% of the meteorological disasters in Xinjiang province which is a key area of the Silk Road Economic Belt over CA, and average of 45 local rainstorms and floods are recorded every year. Improving understanding and forecasting techniques of extreme precipitation over CA induced by multi-scale systems is therefore of great importance.

Sub-tropical westerly jet and its forced secondary circulation and interactions among troughs at high and low levels trigger extreme precipitation with environmental background of synoptic scale. Distinct

---

[*] Corresponding author at: Key Laboratory of Meteorological Disaster (KLME), Ministry of Education & Collaborative Innovation Center on Forecast and Evaluation of Meteorological Disasters (CIC-FEMD), Nanjing University of Information Science & Technology, Nanjing 210044, China

E-mail address: 003542@nuist.edu.cn (J. Cao).

[1] Shuping Ma and Jie Cao have contributed equally to this study.

https://doi.org/10.1016/j.atmosres.2022.106079
Received 25 September 2021; Received in revised form 6 February 2022; Accepted 7 February 2022

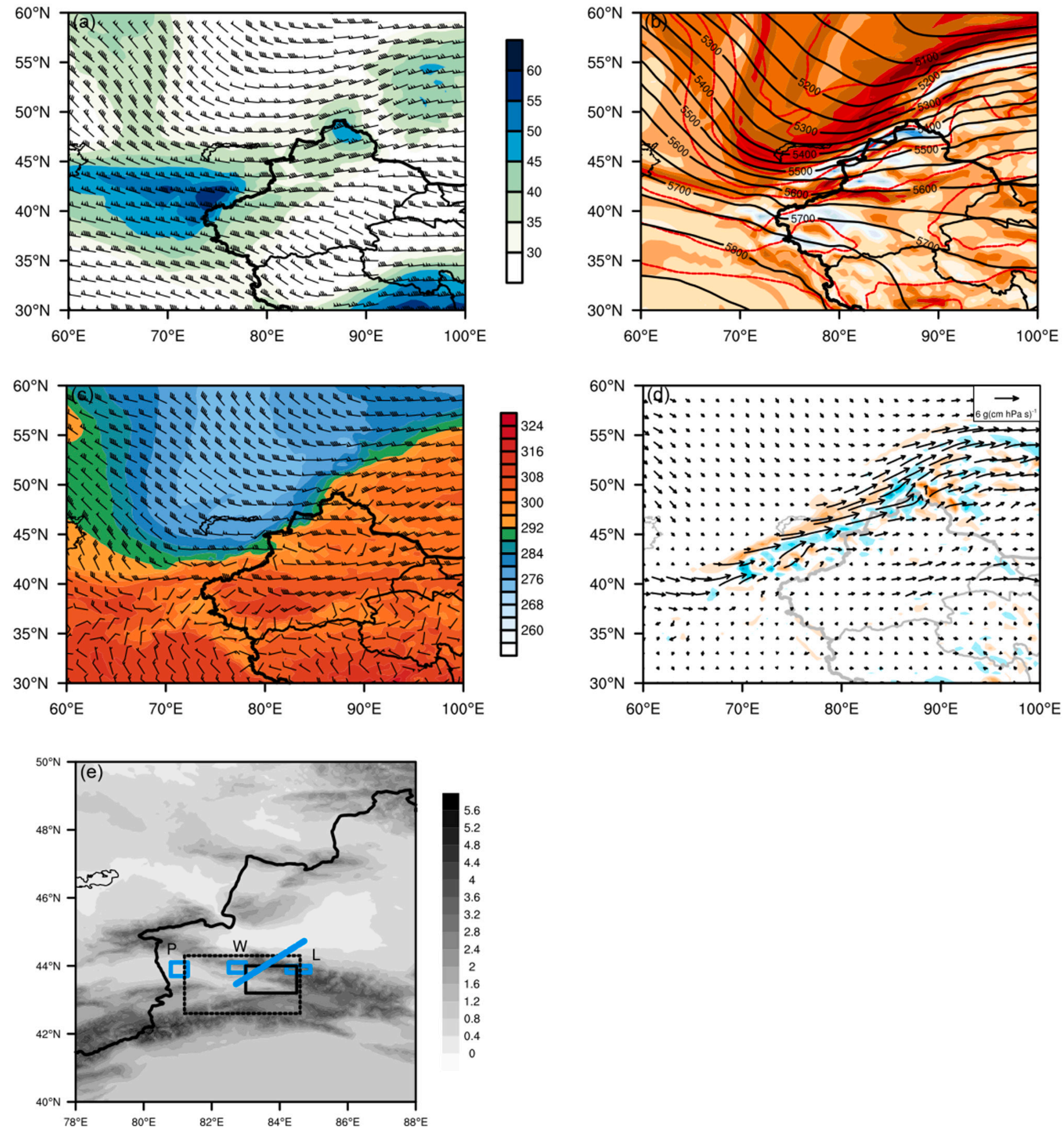

Fig. 1. (a) Wind vector and velocity greater than 30 m s^{-1} (shaded) at 200 hPa at 12 UTC 30 Nov, 2018; (b) geopotential (solid contours, units: gpm), temperature (dashed contours, units: K), and relative vorticity (shaded, units: 10^{-4} s^{-1}) at 500 hPa; (c) wind vector and equivalent temperature (shaded, units: K) at 700 hPa; (d) Water vapor transport (vector, units: g cm^{-1} hPa^{-1} s^{-1}) and its divergence (shaded, units: 10^{-7} g cm^{-2} hPa^{-1} s^{-1}); (e) terrain height from WRF's simulated data (shaded, units: km) with targeted domains marked in W for windward slope and L for lee side in blue rectangular. (For interpretation of the references to colour in this figure legend, the reader is referred to the web version of this article.)

from extreme precipitation events over regions governed by typical monsoon climate, Central Asian vortices of sub-synoptic scale along with Tianshan Mountain stationary front account for 60% torrential precipitation events over Xinjiang (Yang et al., 2015; Guo et al., 2021). In addition, mesoscale-β convective clouds, mesoscale-γ convective clouds and mesoscale convergence lines are directly responsible for local extreme rainstorms in Xinjiang. Characterized by a combination of these weather systems of different scales and fast evolving mesoscale systems, torrential precipitation events over CA are hard to predict with traditional weather analysis tools.

Flow decomposition approach is a powerful technique to separate multi-scale flows. For synoptic up to climatic analysis, statistical tools are utilized by averaging over time or space to partition stationary and transient components (Zhou and Yu, 2005; Yuan et al., 2020). Barnes filter (1964) is adopted to extract synoptic or geostrophic components from total flow in the study of diurnal precipitation in Meiyu front (Xu et al., 2017; Xue et al., 2018). For mesoscale to synoptic studies, flow decomposition firstly originates from PV concept by Hoskins et al.

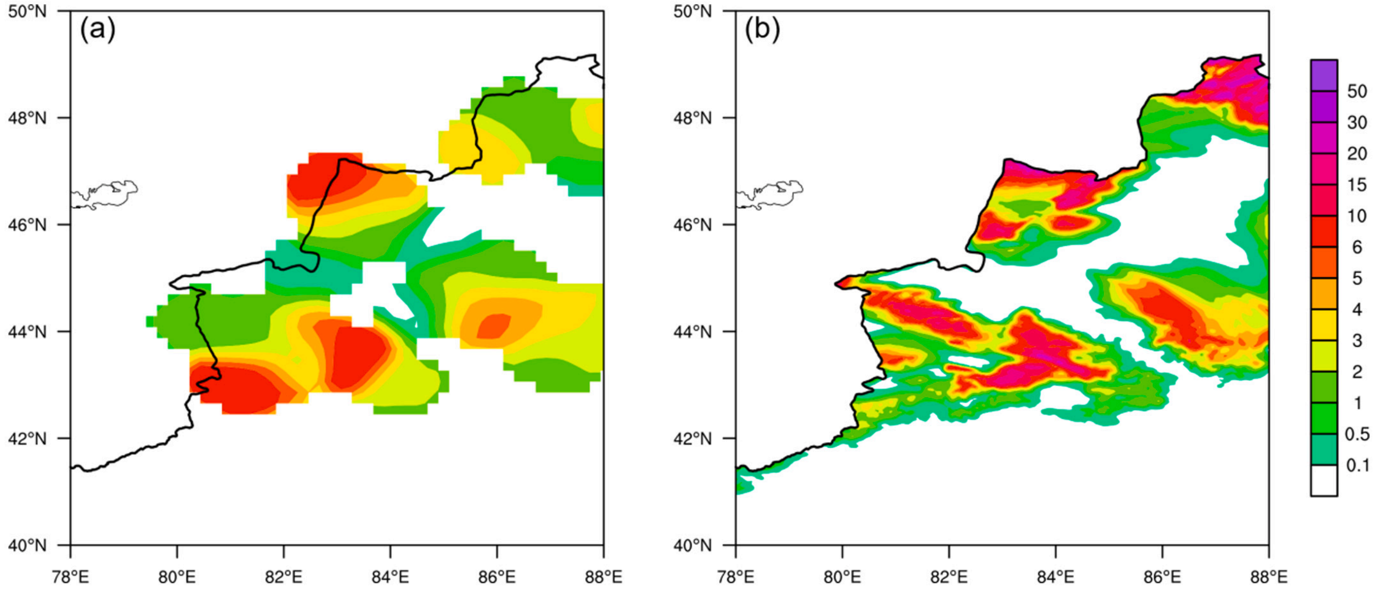

Fig. 2. (a) The 12 h accumulated observed precipitation, and (b) the simulated one at 00UTC on 1 Dec. Units are mm.

(1985) with solid physical foundation. However, mathematical difficulties in solving balanced models and choices of dynamic approximations for extreme events limit its applicability and popularity in operational predictions. The Helmholtz theorem as a simple decomposition method separates wind into rotational and divergent components (Hawkins and Rosenthal, 1965). The rotational flow component describes the large-scale movement and can directly be linked to geopotential, while the divergent one depicts ageostrophic or sub-synoptic motions. It has been widely used in atmospheric and oceanic circulations (Krishnamurti, 1968; Fu et al., 2017; You and Fung, 2019; Ullah et al., 2020, 2021), and data assimilations (Daley, 1991; Parrish and Derber, 1992; Xu et al., 2006, 2007).

Anomalous precipitation is directly related to the moisture supply, and can be represented by water vapor transport which is well studied and widely used over the global (Trenberth and Guiliemot, 1995) and over East Asia and South Asia (Ding, 1994; Huang et al., 1998; Simmonds et al., 1999; Zhang, 2001; Zhou and Yu, 2005; Wang et al., 2021). Dimego and Bosart (1982) partition the water vapor flux components to examine the relative importance of moisture budgets in a tropical storm. Shi et al. (2008) quantitatively investigate the input, output and net water vapor transports at different levels in troposphere over Xinjiang Province from the perspective of annual and seasonal scales. Case studies also show influences of interactions between water vapor transport channels and governing weather systems on locations and intensities of precipitation (Zeng and Yang, 2020).

As we know, terrain effects on extreme precipitation have been investigated theoretically and numerically (Tripoli and Cotton, 1989; Schumacher and Johnson, 2008; Wang et al., 2016; Adhikari and Liu, 2019; Hua et al., 2020) with conclusions of mountainous flows differing worldwide due to the geometry of terrain as well as distinct environmental circulations. Studies in East China and North China are more mature with intense observations, while orographic precipitation events over Xinjiang have recently been investigated. Since the mountainous area of Tianshan accounting for 40.4% of the total precipitation in Xinjiang (Shi et al., 2008), terrain effects are not negligible. Ili Valley is a typical region in CA featuring in a trumpet-like topography facing west which is easier to gather water vapor. Distributions and characteristics of water vapor transports and aggregations on both windward slope and lee side are diagnosed with decomposed water vapor flux divergence to identify terrain influences.

In this study, water vapor flux divergence will be partitioned and analyzed in the perspective of relative importance of its decomposed components on a blizzard over different regions of the complicated Ili Valley. Methodology of flow decomposition technique in water vapor flux divergence under terrain-following coordinate systems is derived in next section. Case overview of the extreme snowstorm is described in Section 3. In Section 4, relationships between partitioned water vapor flux divergence and locations and intensity of precipitation are investigated in comparisons to the original undecomposed one. Conclusions and discussions are in Section 5.

2. Methodology

According the Helmholtz theorem, a horizontal velocity field **v** can be partitioned into rotational and divergent components represented by streamfunction ψ and velocity potential χ, respectively, as follows:

$$\mathbf{v} = \mathbf{v_r} + \mathbf{v_d}, \tag{1}$$

$$\mathbf{v_r} = \mathbf{k} \times \nabla\boldsymbol{\psi}, \tag{2a}$$

$$\mathbf{v_d} = \nabla\boldsymbol{\chi}, \tag{2b}$$

where **k** is the unit vector in the vertical direction and ∇ is the horizontal gradient operator. For a limited domain D, the following relationships hold as:

$$\nabla^2\psi = \zeta \text{ in } D, \tag{3a}$$

$$\nabla^2\chi = \alpha \text{ in } D, \tag{3b}$$

$$\partial_n\psi + \partial_s\chi = v_s \text{ along } \partial D, \tag{4a}$$

$$\partial_n\chi - \partial_s\psi = v_n \text{ along } \partial D. \tag{4b}$$

Here ζ and α are the vorticity and divergence, respectively. ∂D denotes the boundary of domain D. v_s and v_n are the boundary-tangential and boundary-normal velocity along ∂D. The accurate integral scheme (Xu et al., 2011) is used to solve for ψ and χ. Applicability and efficiency for flows with boundary values of arbitrary spatial variations are the strength of this method which is suitable for limited areas over complex terrains such as Ili Valley in the next subsection.

The Eulerian atmospheric water budget equation for an atmospheric column of unit area (Yanai et al., 1973; Ninomiya and Kobayashi, 1999; Sun and Wang, 2014, 2015) is adopted as follows:

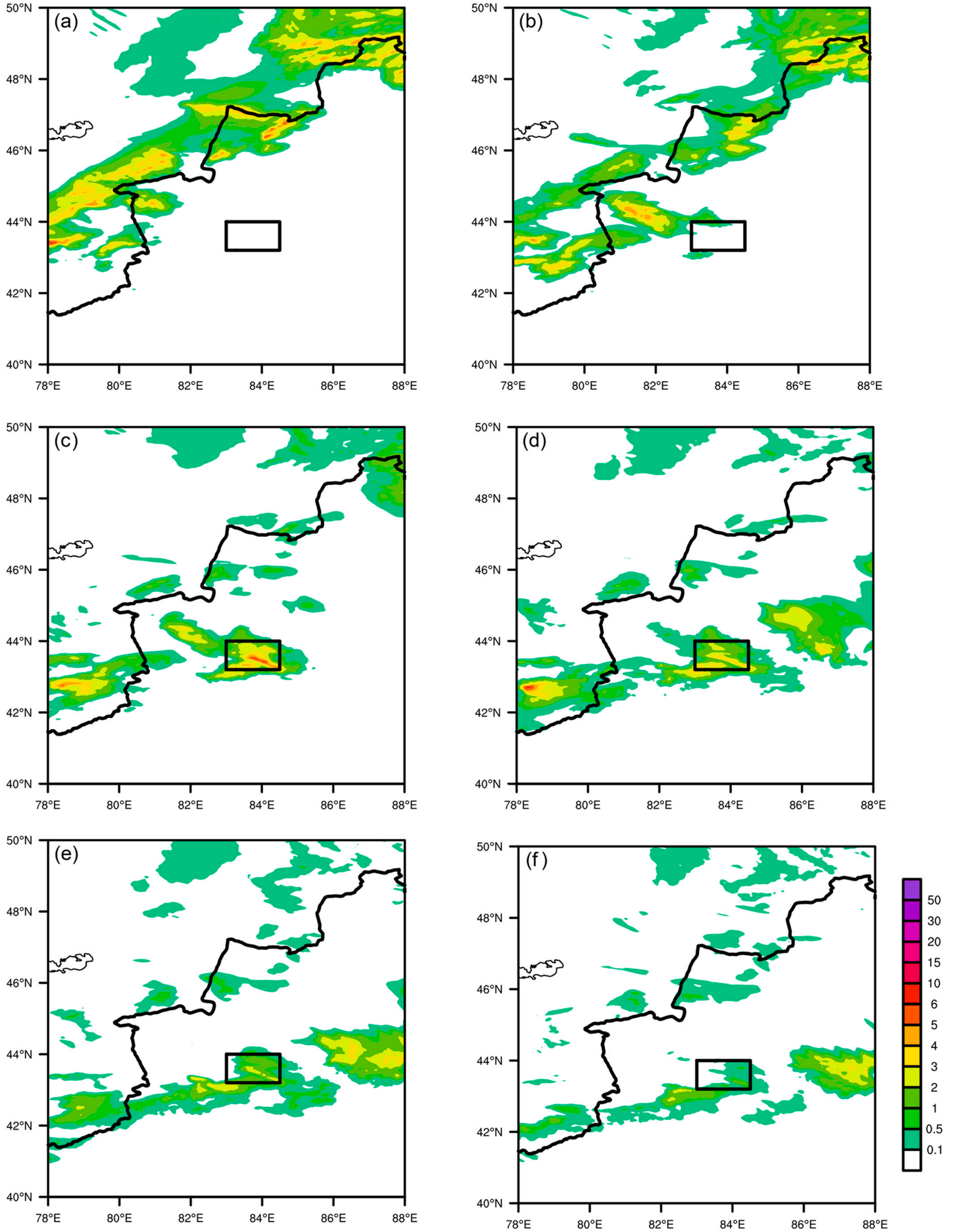

Fig. 3. The simulation of 1 h accumulated precipitation at (a) 1600UTC, (b) 1800UTC, (c) 20UTC, (d) 22UTC on 30 Nov, and at (e) 00UTC, (f) 02UTC on 1 Dec. Units are mm.

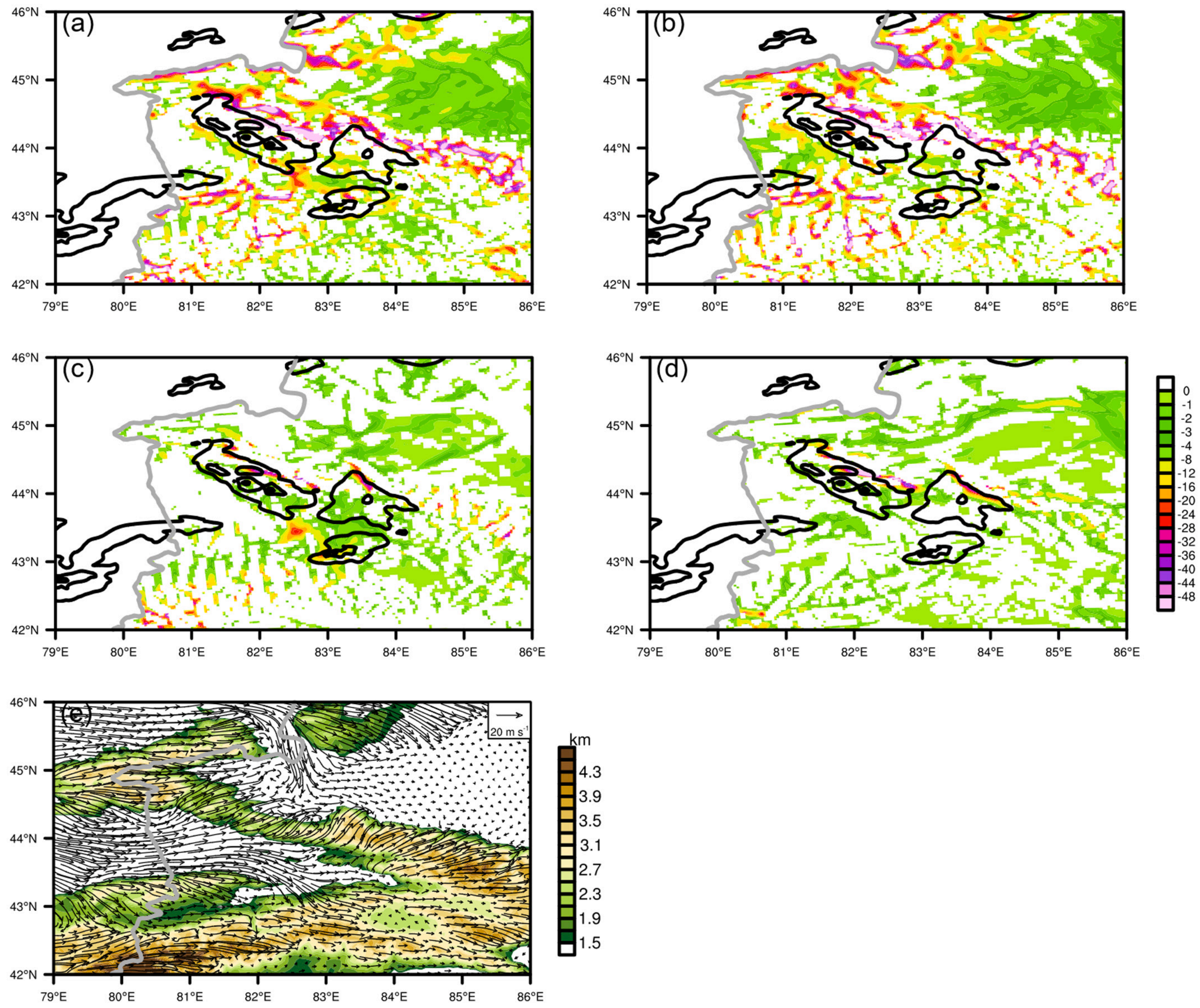

Fig. 4. Vertical integral of (a) Q_v^{all}, (b) Q_v^{div}, (c) Q_v^{L}, (d) Q_v^{S} in the unit of 10^{-8} g cm^{-2} hPa^{-1} s^{-1}, and (e) streamlines of wind field at 0.9558 overlaid by terrain heights (shaded, units: mm) at 1700UTC, black contours are the simulation of 1 h accumulated precipitation (units: mm) at 1900 UTC on 30 Nov.

$$(1/g)\int_{ps}^{0} \partial_t q \, dp + (1/g)\int_{ps}^{0} \left[\nabla\cdot(q\mathbf{v}) + \partial_p(q\omega)\right] dp = P\text{–}E, \qquad (5)$$

where q represents specific humidity, P and E indicate the precipitation and the evaporation from the underlying surface, respectively. Vertical integration is performed between the surface pressure, p_s, and top. Due to the impenetrability of the atmosphere, ω vanishes at the surface and the top. Eq. (5) becomes:

$$(1/g)\int_{ps}^{0} \partial_t q \, dp + (1/g)\int_{ps}^{0} \nabla\cdot(q\mathbf{v}) \, dp + E = P. \qquad (6)$$

The first term in the left-hand-side of Eq. (6), $\partial_t q$, represents the difference between q at two successive times. According to the literatures on the water vapor flux budget (Murakami, 1959; Ninomiya and Akiyama, 1971; Ding, 1993; Ninomiya and Kobayashi, 1999), it is relatively small over an area bounded within two meridians and latitude circles. The third term in the left-hand-side of Eq. (6) can be calculated using the bulk aerodynamic formula (Fairall et al., 2003; Gao et al., 2017):

$$E = \rho_a C_E U \left[q_{\text{sat}}\,(\text{SST}) – q_a\right],$$

where ρ_a is the air density, C_E is the turbulent exchange coefficient for moisture, U is the 10-m wind speed, q_{sat} (SST) is the saturation specific humidity at the SST, and q_a is the 10-m specific humidity. For the studies of the winter precipitation over a small domain with short duration, the influence of E on Eq. (6) is less important than the vertically integrated water vapor flux divergence. In this study of mesoscale analysis with short duration, the other terms in Eq. (6) are less important to P and thus will not be considered from now on. The second left-hand-side term is the vertically integrated water vapor flux divergence which is directly related to moisture budgets and responsible for anomalous precipitation (Dimego and Bosart, 1982; Zhou and Yu, 2005). The expression for the integrand under pressure coordinates is:

$$\nabla\cdot(q\mathbf{v})\,|_p \qquad (7)$$

Here, the subscript p represents variables in pressure coordinate systems. Substituting Eq. (1) into Eq. (7) leads to:

$$\nabla\cdot(q\mathbf{v})|_p = q\nabla\cdot\mathbf{v}\big|_p + \mathbf{v}_r\cdot\nabla q\big|_p + \mathbf{v}_d\cdot\nabla q\big|_p \qquad (8)$$

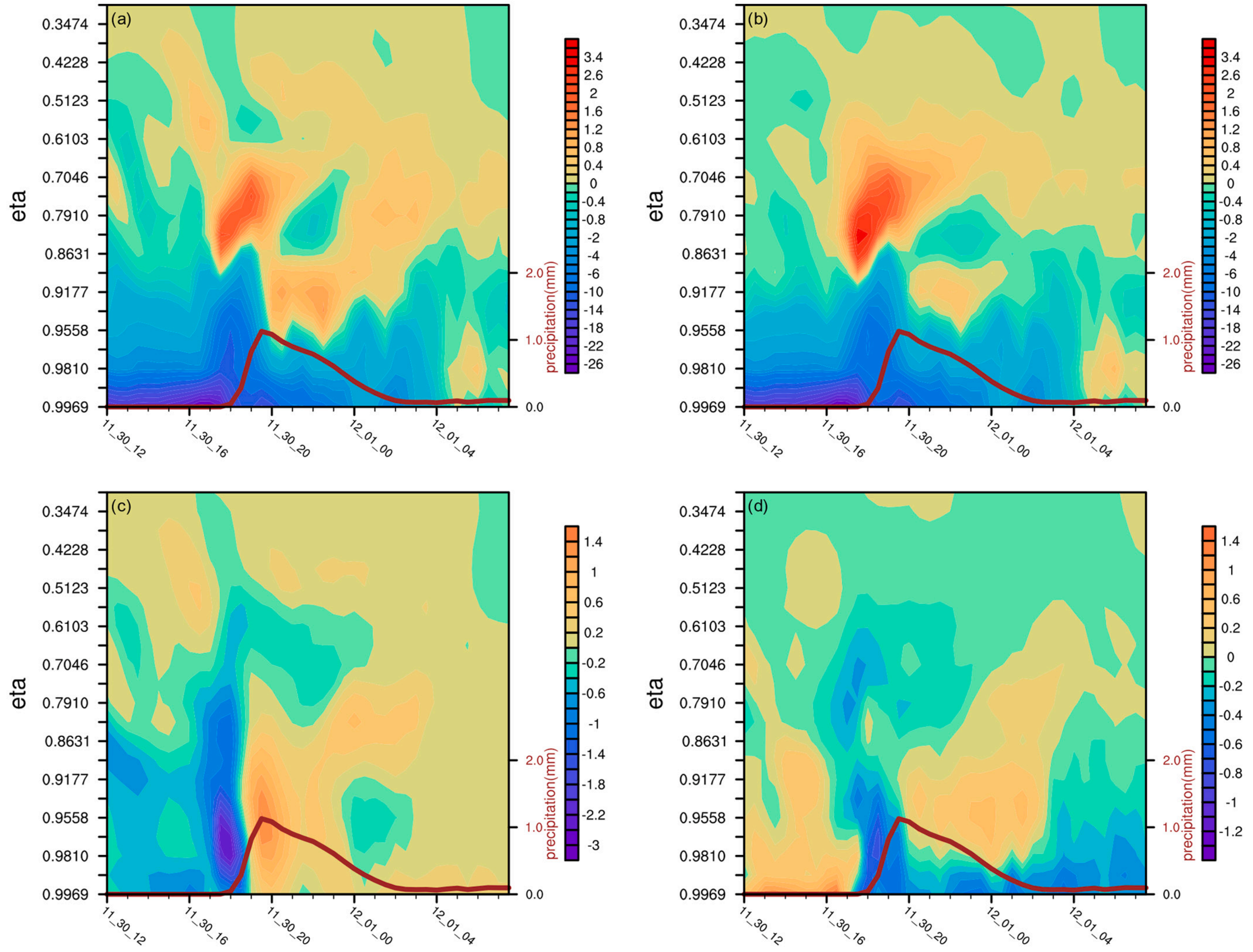

Fig. 5. Domain averaged (a) Q_v^{all}, (b) Q_v^{div}, (c) Q_v^{L}, and (d) Q_v^{S} (shaded) in the unit of 10^{-7} g cm^{-2} hPa^{-1} s^{-1}. Brown curves represent precipitation with values in the right y-axis in the unit of mm. The target domain is marked in solid lines in Fig. 1e. (For interpretation of the references to colour in this figure legend, the reader is referred to the web version of this article.)

Use the coordinate conversion formula (Cao and Xu, 2011) to write (8) into the terrain-following pressure coordinate system,

$$\partial_p A = (\partial_\eta A)(\partial_p \eta) \tag{9}$$

$$(\partial_s A)|_\eta = (\partial_s A)|_p + (\partial_p A)(\partial_s p)|_\eta \tag{10}$$

Here the subscript η is the vertical axis in terrain-following coordinate system. Substituting Eqs. (9) and (10) into Eq. (8) leads to:

$$\begin{aligned}\nabla\cdot(q\mathbf{v})|_p &= (\partial_x qu)|_p + (\partial_y qv)|_p \\ &= (\partial_x qu)|_\eta + (\partial_y qv)|_\eta - [(\partial_p qu)(\partial_x p)|_\eta + (\partial_p qv)(\partial_y p)|_\eta]\end{aligned} \tag{11}$$

$$(q\nabla\cdot\mathbf{v})|_p = q\partial_x u|_p + q\partial_y v|_p = q\partial_x u|_\eta + q\partial_y v\Big|_\eta - q[(\partial_p u)(\partial_x p)|_\eta + (\partial_p v)(\partial_y p)|_\eta] \tag{12}$$

$$\begin{aligned}(\mathbf{v}_r\cdot\nabla q)|_p &= u_r\partial_x q|_p + v_r\partial_y q|_p \\ &= u_r\partial_x q|_\eta + v_r\partial_y q|_\eta - u_r(\partial_p q)(\partial_x p)|_\eta - v_r(\partial_p q)(\partial_y p)|_\eta\end{aligned} \tag{13}$$

$$\begin{aligned}(\mathbf{v}_d\cdot\nabla q)|_p &= u_d\partial_x q|_p + v_d\partial_y q|_p \\ &= u_d\partial_x q|_\eta + v_d\partial_y q|_\eta - u_d(\partial_p q)(\partial_x p)|_\eta - v_d(\partial_p q)(\partial_y p)|_\eta\end{aligned} \tag{14}$$

The non-divergent property of $\mathbf{v_r}$ is used in the above derivation. Water vapor flux divergence (denoted by Q_v^{all}) is thus partitioned into three components as: flow divergence (denoted by Q_v^{div}), moisture convection term by non-divergent or large-scale motions (denoted by Q_v^{L}) and by divergent or sub-synoptic scale motions (denoted by Q_v^{S}). The locations and intensities of Q_v^{all} are commonly used to represent precipitations in many cases of traditional weather analysis and climatological studies. However it fails in extreme events influenced by multi-scale weather systems and complex terrains. In the following sections, their quantitative values on windward slope and lee side of mountain will be evaluated to see their relative importance to moisture aggregations in different periods during a specific blizzard event.

3. Case overview

A snowstorm hits Xinjiang Province during 30 November to 1 December 2018 and brings heavy precipitation to Ili Valley in 8 h before heading eastwards. The severe blizzard over Ili Valley is the target of the following analysis with the hourly reanalysis dataset ERA5 (Hersbach et al., 2018). Large-scale environmental allocations at 1200 UTC 30 Nov are depicted in Fig. 1. The exit region of high level jet dominates most parts of Xinjiang province with divergent flow at 200 hPa. The southwest warm moist air flow in front of the trough at 500 hPa passes

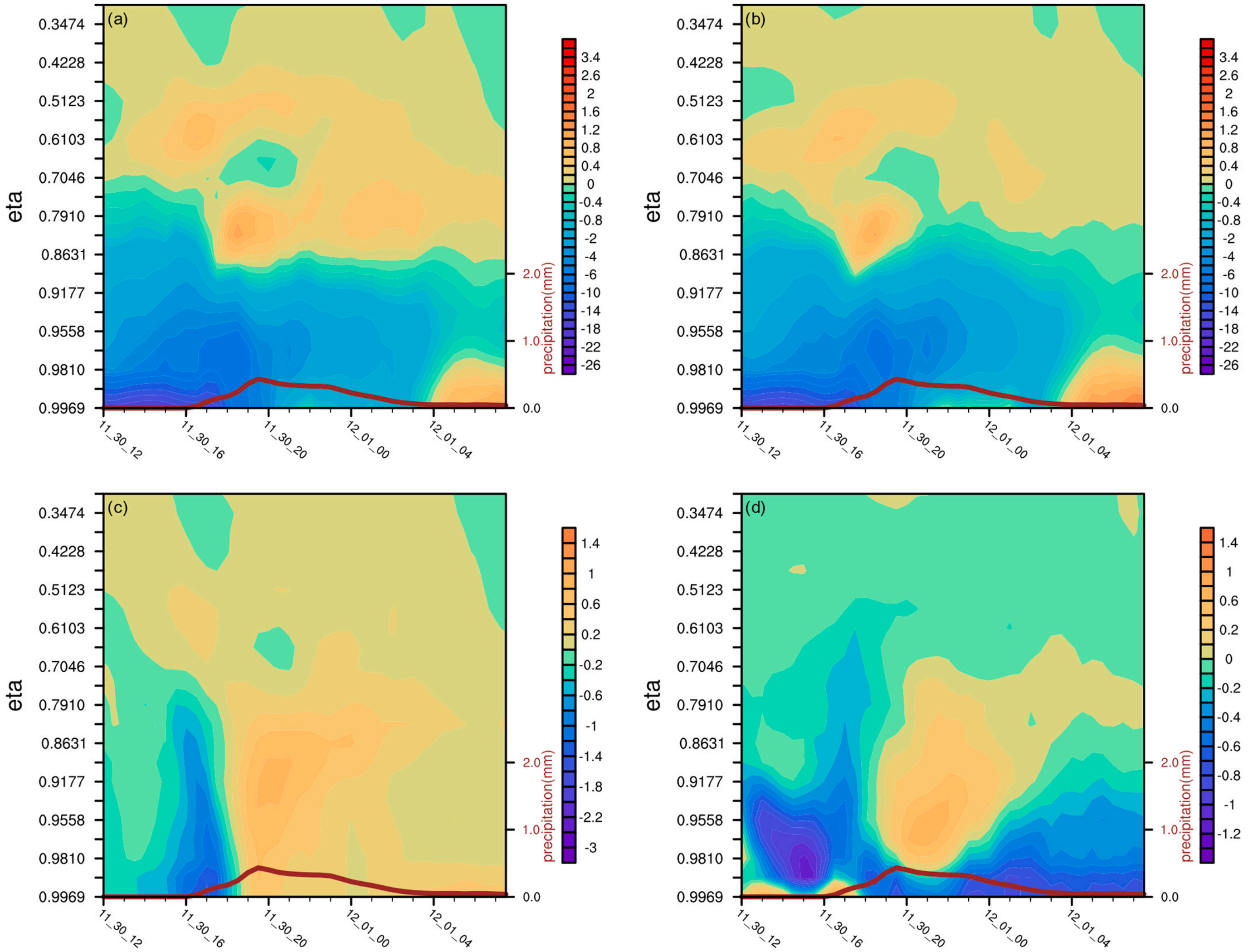

Fig. 6. Same as Fig. 4, but for the target domain in dashed lines in Fig. 1e.

through Ili Valley when precipitation starts. Westerly at 700 hPa is prevailing with convergent regions distributing over Ili Valley and south slope of Tianshan Mountain due to orographic lifting. Cold front can be seen from the dense contours of equivalent potential temperature. The eastward water vapor transport path brings moisture from Balkhash Lake to Ili Valley. Allocations of these large-scale systems are favorable for the initiating of blizzard, but weak negative Q_v^{all} zones are not finely associated with precipitation.

National Center of Atmospheric Research's WRF model (Skamarock and Coauthors, 2008) is used to reproduce this blizzard. This simulation takes the US NCEP GFS (National Centers for Environmental Prediction Global Forecast System) forecast field data as the background field and side boundary conditions and uses GSI (Gridpoint Statistical Interpolation analysis system) to assimilate the GDAS (Global Data Assimilation System) observation data. The model area adopts a single-layer grid design with a horizontal resolution of 3 km. The simulation time is from 00UTC 30 Nov to 00UTC 2 December with output once every 30 min. Thompson (cloud microphysics scheme), RRTMG (longwave and shortwave radiation scheme), Yonsei University scheme (planetary boundary layer scheme), Mellor-Yamada-Janjic TKE scheme (Surface layer scheme) and Noah Land Surface Model (land surface scheme) are used in this simulation. Detailed configurations and accuracy tests of this simulation may refer to Ma et al. (2021). Though stronger in intensity than the observed precipitation (Fig. 2), the temporal evolution of the simulated snowstorm well resembles observations (Figures omitted). Simulated storm at 1600UTC 30 Nov first arises at the north slope of Tianshan Mountain in the upstream of Ili Valley (Fig. 3a). The snowstorm moves eastward to Ili Valley changing its pattern parallel to terrain in the next 2 h with maxima precipitation locating on windward slope. At 2000UTC, precipitation zones expand with maxima snow centers arising to the east of the Valley. The extreme precipitation occupies Ili Valley during 2100UTC to 23UTC. On Dec. 1, the simulated snowstorm moves out of the target domain encircled by solid black lines in Fig. 1e.

4. Analyses of decomposed water vapor flux divergence

4.1. Horizontal variations

Correlations between allocations of 1 h accumulative precipitation (Fig. 3) and Q_v^{all} and its decomposed components are investigated during the entire life cycle of the blizzard over Ili Valley. Similar to Q_v^{all} at 850 hPa as shown in Fig. 1d, vertically integrated Q_v^{all} from near surface to around 3 km above surface (Fig. 4a) diverges in the precipitating area at 1700 UTC while precipitation arises on windward slope north and west to Ili Valley at 1900 UTC 30 Nov. At that time, negative values of Q_v^{div} (Fig. 4b) aggregate along the lee side corresponding to strong convergence after flow climbs across the mountain (Fig. 4e). The alignment of snowstorm 2-h lagging is identical to distributions of Q_v^{L} (Fig. 4c) with extreme precipitation centers lags by 2 h overlapping large

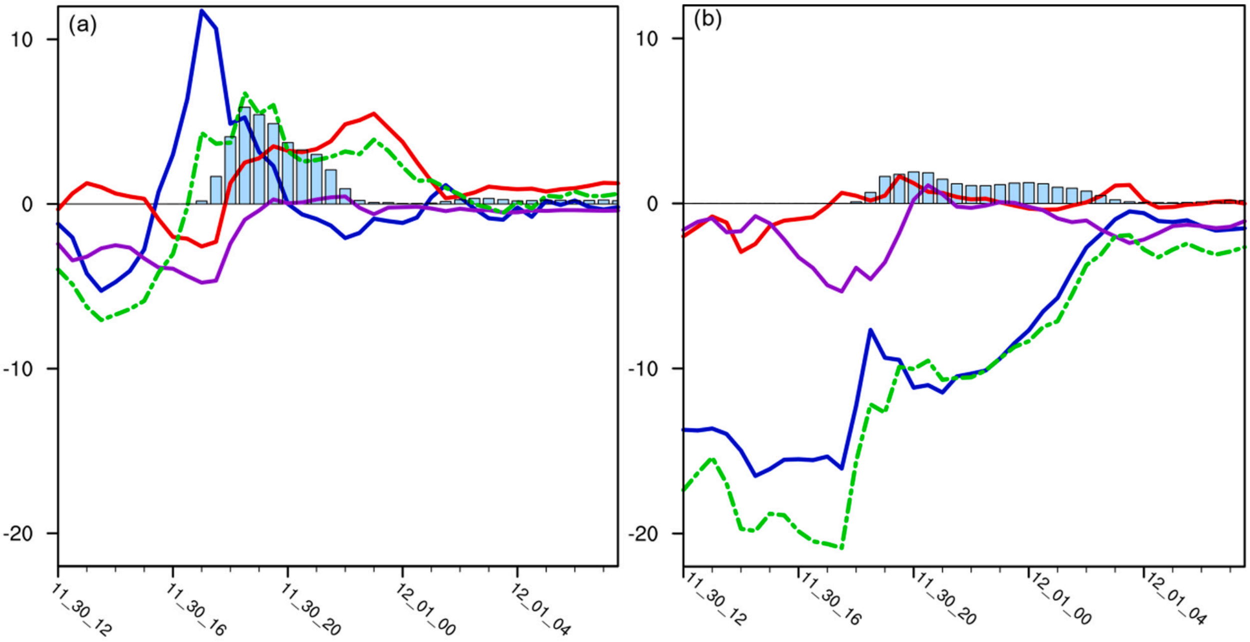

Fig. 7. Vertical integral of Q_v^{all} (dashed green lines), Q_v^{div} (blue lines), Q_v^{L} (red lines), and (d) Q_v^{S} (purple lines) in the unit of 10^{-8} g cm^{-2} hPa^{-1} s^{-1} on (a) windward slope and (b) lee side. Precipitation is depicted in light blue histogram in the unit of 10^{-1} mm. (For interpretation of the references to colour in this figure legend, the reader is referred to the web version of this article.)

negative centers of Q_v^{L} and Q_v^{S}. As the westerly continues to climb the slope, precipitation belt moves across Ili Valley and distributes east and south to the mountainous region. Main convergent areas of Q_v^{div} (figures omitted to avoid repetition) still occupy lee side instead of the main rain belt, while Q_v^{L} remains the same pattern with precipitation zone with maximum values overlapping lagging snow centers.

As a short conclusion, both Q_v^{L} and Q_v^{S} are indicative of the beginning and weakening of precipitation. The convergent flow induced by topography over Ili Valley occupies large area mostly on lee side and fails to represent moisture convergences when precipitation arises or moves eastward. It is larger in magnitude than the summation of the other two components and therefore eliminates their indications for moisture aggregations, and results in failing to reveal precipitation from undecomposed Q_v^{all}.

4.2. Time-height variations

As analyzed in last subsection, horizontal evolutions of decomposed water vapor flux convergence are better associated with intensity and movement of the blizzard. Temporal variations of their vertical distributions may give more clues to mechanisms of water vapor transports among different levels since this blizzard is under favorable synoptic backgrounds up to 200 hPa. As can be seen in Fig. 5a, distributions of domain averaged Q_v^{all} over the solid black rectangular present evident convergent features at lower and middle levels whether the precipitation starts or weakens. Vertical transports of divergent Q_v^{all} at middle and high levels are obstructed by large and intense convergent regions at lower and middle levels. It is mainly caused by the convergent flow field at lower and middle levels during the entire blizzard event and divergent flow at middle and high levels depicted by Q_v^{div} (Fig. 5b). Q_v^{L} (Fig. 5c) at lower and middle levels presents large areas of intense negative values before the precipitation reaches its maximum. This convergence is mainly due to the jet exit at 200 hPa, northwest warm moist airflow by trough at 500 hPa, and secondary circulations triggered by cold front at 700 hPa. Q_v^{L} weakens when the snowstorm moves out of the target domain since 2000 UTC 30 Nov. Strong convergence is seen in Q_v^{S} (Fig. 5d) at lower and middle levels before the precipitation reaches its maximum. While the snowstorm in the target domain becomes weaker, a divergent lid blocks the relatively large convergent center at middle levels and convergence in lower level becomes weaker.

Similar conclusions for Q_v^{all} and Q_v^{L} remain after enlarging the target domain to the dashed rectangular. As seen in Fig. 6, the convergent regions of Q_v^{all} are still at lower and middle levels weather before storm arises or after precipitation weakens. Q_v^{L} presents consistent negative or positive values prior to the increase or decrease of precipitation. Similar to the smaller domain, deep and massive convergent wind fields in Q_v^{div} at lower and middle levels are the reason for the convergence in Q_v^{all} during the entire blizzard event. When the convergent flow weakens as the rain belt moves out of the larger domain, Q_v^{div} is dominated by weaker convergent flow. The convergent regions of Q_v^{S} are strong before precipitation starts and diminish instantly when the snowstorm moves out of the domain with water vapor flux convergence occupying at lower levels subsequently.

The similarity among the two target domains proves the necessity for decomposing Q_v^{all} to see relative importance of Q_v^{L}, Q_v^{S}, and Q_v^{div} in identifying moisture aggregation and dispersion at different heights. Differences are resulted from the complicity of terrains over Ili Valley. The smaller domain only contains Valley and windward slope, while the larger one contains both windward slope and lee side of Tianshan Mountain. Vertical integrals of decomposed terms over different types of topography will be analyzed individually in the next subsection.

4.3. Characteristics on windward slope and lee side

From Fig. 7a, we can see that the undecomposed Q_v^{all} remains positive prior to the blizzard, which fails to indicate moisture convergence on windward slope. Moisture convergence during the blizzard is mainly due to the excessively large divergence of Q_v^{div} which counteracts the contributions of convergent Q_v^{L} and Q_v^{S}. The latter two components have the same magnitude which is a half of Q_v^{div}. All three components increase or decrease as precipitation arises or abates. Q_v^{L} represents large-scale weather systems which are favorable for precipitation from conventional analysis shown in Fig. 1a–c. It can also be seen from simulated black body temperature (denoted as TBB in Fig. 8) that a large convective banded structure is moving eastward across the target domain. The horizontal extension of the cloud cap seen from the

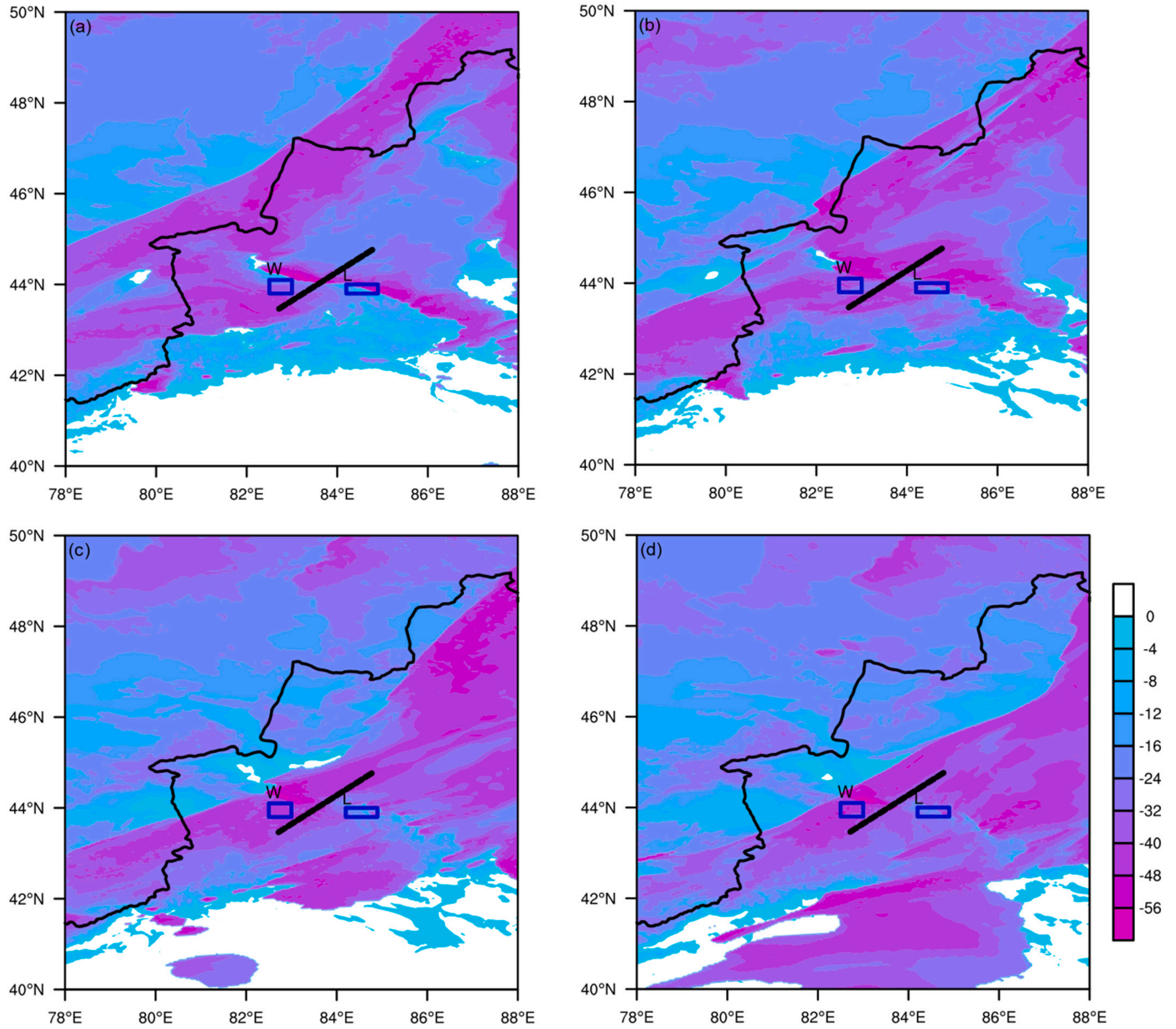

Fig. 8. Simulated Black body temperature (TBB) at (a) 1800UTC, (b) 2000UTC, (c) 2200UTC on 30 Nov, and at (d) 0000 UTC on 1 Dec. Units are K.

precipitable hydrometeor mixing ratio (solid contours in Fig. 9) on windward slope also indicates the approach of large-scale systems to the terrain. Q_v^S is consistent with the allocation of vertical velocity on windward slope induced by orographic gravity waves (Ma et al., 2021) as shown in Fig. 9.

Flow converges after climbing across the mountain, leading to large negative values of Q_v^{div} on lee side in Fig. 7b. Q_v^L suppresses local moisture convergence with positive values 1 h prior to precipitation mainly due to the topographic blocking. It can be seen in Fig. 9 that the cloud cap fails to extend to the lee side by downhill wind. A slight decreasing trend can be seen in Q_v^L when the blizzard event starts. The contribution of Q_v^S to precipitation ahead of the event is due to the vertical lifting induced by orographic gravity waves as shown in Fig. 9. For the same reason, snow terminates as vertical lifting weakens on lee side. Same as on windward slope, the magnitude of Q_v^{div} doubles the summation of Q_v^L and Q_v^S. The undecomposed Q_v^{all} on lee side is therefore still dominated by Q_v^{div} while well depicts water vapor aggregation and thus fails to indicate the end of the blizzard. On the contrary, Q_v^L and Q_v^S contribute to the moisture divergence as snowstorm gradually weakens.

Therefore decomposition of Q_v^{all} is of significant importance in analyzing moisture aggregation on windward slope governed by divergent flow, and moisture dispersion on lee side governed by convergent flows.

5. Conclusions and discussions

Central Asia is one of the largest arid and semi-arid regions in the world where precipitation plays a vital important role in agricultural and economic developments. Intensive studies have been performed on characteristics of precipitation over Central Asia from the perspective of climatic scale and diurnal evolutions. Xinjiang Province, as an important region in CA, is experiencing an increase in occurrence of extreme precipitation events which lead to severe hydrological threats, tremendous social and economic losses. Caused by multi-scale weather systems and complex topography, extreme events are hard to predict with traditionally used tools. Detailed comprehension of the relationship between water vapor transport by different scales of motions and severe

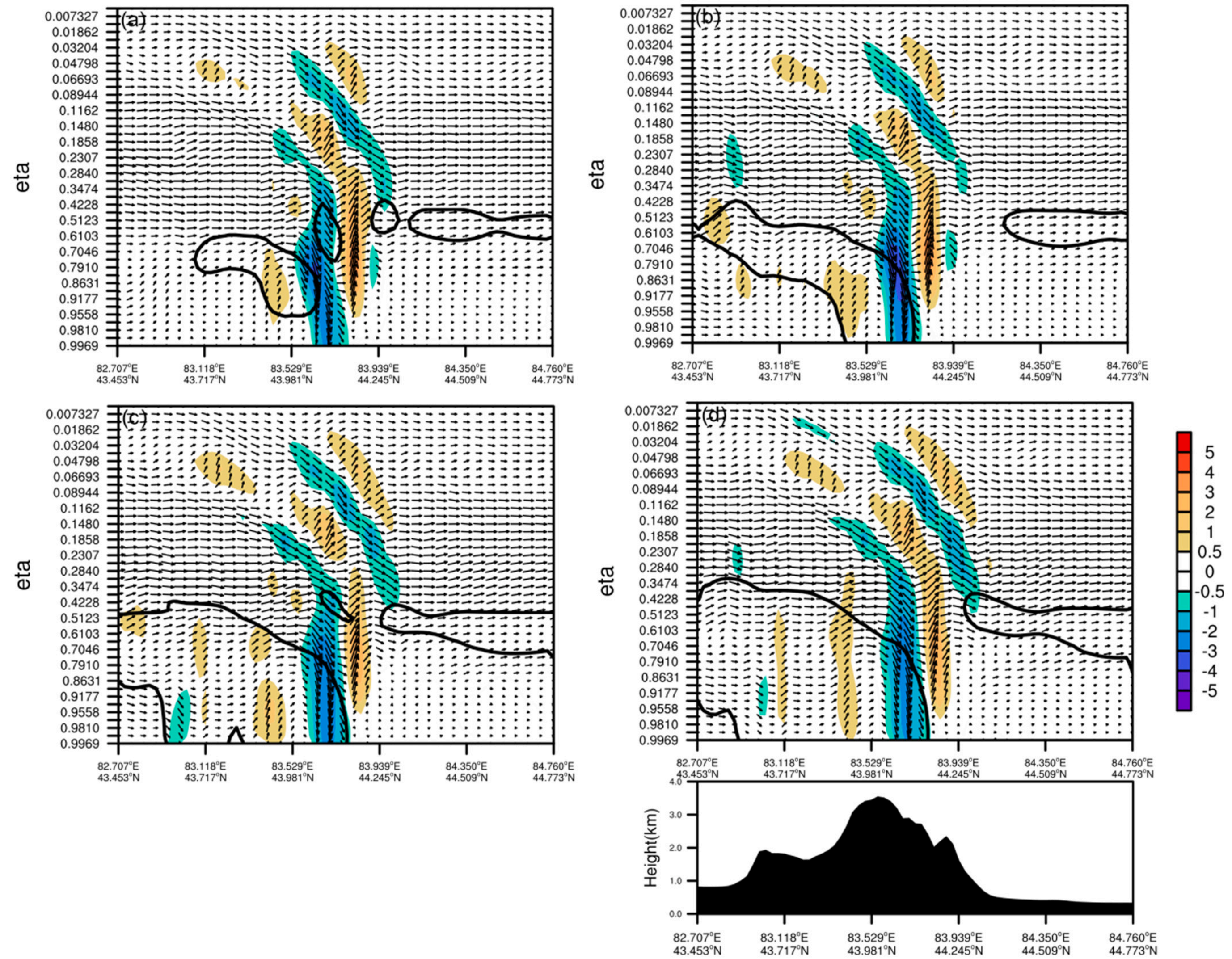

Fig. 9. Cross section of the precipitable hydrometeor mixing ratio (black lines, units: 10^{-4} kg/kg), vertical velocity (shaded, units: m s^{-1}), and wind vector of (u, w) at (a) 1700UTC, (b) 1730UTC, (c) 1800UTC, and (d) 1830UTC along the dashed blue line in Fig. 1e. Terrain heights of the cross section are attached below the last panel. (For interpretation of the references to colour in this figure legend, the reader is referred to the web version of this article.)

storms under complex terrains over Ili Valley, a typical region in Central Asia, has been an issue of considerable urgency.

Flow decomposition technique is powerful in both climatic and synoptic analysis. By utilizing the Helmholtz theorem, the total water vapor flux divergence (Q_v^{all}) is partitioned into three components as: flow divergence (Q_v^{div}), moisture transport by large-scale motions (Q_v^L) and by sub-synoptic scale motions (Q_v^S). Traditionally used successive over-relaxation method is adopted in the mathematical calculation. In this study, a blizzard event over Ili Valley in the winter of 2018 is analyzed first with synoptic background and then with high-resolution numerical simulation. Decomposed components are investigated focusing on their relative importance in identifying water vapor aggregation on windward slope and lee side of Tianshan Mountain. Comparative analyses to the convergence of total water moisture budgets are concluded as follows:

(1) Both Q_v^L and Q_v^S converge prior to precipitation, and diverge or weaken as the blizzard ends. Q_v^L performs better on windward slope and represents vertical transports from upper levels, while Q_v^S achieves better in indicating precipitation occurring on lee side.

(2) Q_v^{div} diverges ahead of precipitation starts on windward slope and thus eliminates the favorable moisture convergent environment provided by Q_v^L and Q_v^S. On the other hand, Q_v^{div} converges on lee side of mountainous regions and thus destructs the suppression of precipitation seen from Q_v^L and Q_v^S.

(3) As for practical weather forecasting, the arise of negative values in Q_v^L at lower and middle levels on windward slope calls for more attention while its vertical integral is similar to the pattern of rain belt in the next 1 or 2 h. Q_v^S which relates to orographic gravity waves is more important on lee side.

As intensive observational experiments of the mesoscale systems and cloud physical characteristics of extreme precipitation have been conducted over Ili Valley with a standard sharing platform, the relative importance of partitioned water vapor flux components with high resolution observations is supposed to have more forecast applications to extreme precipitation events. Applications of this flow decomposition method to summer extreme events in other places with complex terrains and comparative studies of different flow decomposition methods are under research.

Declaration of Competing Interest

The authors declare that they have no known competing financial interestsor personal relationships that could have appeared to influence the work reported in this paper.

Acknowledgements

The authors are thankful to the anonymous reviewers for their comments and suggestions on the original manuscript that improved presentations of the results. The computing for this project was performed at the Supercomputing Center for Education & Research at the University of Oklahoma (OU), USA. This work was supported by the National Key Research and Development Project of China Grant 2018YFC1507104, the National Natural Science Foundation of China Grants 91937301, 41875074 and 41675060, the Second Tibetan Plateau Comprehensive Scientific Expedition 2019QZKK0104, the National Key Scientific and Technological Infrastructure Project “EarthLab”.

References

Adhikari, A., Liu, C., 2019. Geographical distribution of thundersnow events and their properties from GPM Ku-band radar. J. Geophys. Res. 124, 2031–2048. https://doi.org/10.1029/2018JD028839.

Barnes, S.L., 1964. A technique for maximizing details in numerical weather map analysis. J. Appl. Meteorol. 3, 396–409. https://doi.org/10.1175/1520-0450.

Bothe, O., Fraedrich, K., Zhu, X., 2012. Precipitation climate of Central Asia and the large-scale atmospheric circulation. Theor. Appl. Climatol. 108, 345–354. https://doi.org/10.1007/s00704-011-0537-2.

Cao, J., Xu, Q., 2011. Computing rossby potential vorticity in terrain- following coordinates. Mon. Wea. Rev. 139, 2955–2961.

Daley, R., 1991. Atmospheric Data Analysis. Cambridge University Press, p. 457.

Dimego, G., Bosart, L., 1982. The transformation of tropical storm Agnes into an extratropical cyclone. Part II: moisture, vorticity and kinetic energy budgets. Mon. Weather Rev. 110, 412–433. https://doi.org/10.1175/1520-0493.

Ding, Y.H., 1993. Study on the Persistent Heavy Rainfall over the Yangtze River Valley and Huaihe River Basin in 1991. China Meteorological Press, 255pp.

Ding, Y.H., 1994. Monsoons over China. Springer, New York, 90pp.

Duan, W.L., He, B., Takala, K., Luo, P.P., Hu, M.C., Alias, N.E., Nover, D., 2015. Changes of precipitation amounts and extremes over Japan between 1901 and 2012 and their connection to climate indices. Clim. Dyn. 45, 1–20. https://doi.org/10.1007/s00382-015-2778-8.

Fairall, C.W., Bradley, E.F., Hare, J.E., Grachev, A.A., Edson, J.B., 2003. Bulk parameterization of air-sea fluxes: updates and verification for theCOARE3.0 algorithm. J. Clim. 16, 571–591. https://doi.org/10.1175/1520-0442(2003)016<0571:BPOASF>2.0.CO;2.

Fu, S.M., Cao, J., Jiang, X.W., Sun, J.H., 2017. On the variation of divergent flow: an eddy-flux form equation based on the quasi-geostrophic balance and its application. Adv. Atmos. Sci. 34, 599–612. https://doi.org/10.1007/s00376-016-6212-x.

Gao, S., Zhai, S., Chen, B., Li, Tim, 2017. Water budget and intensity change of tropical cyclones over the western North Pacific. Mon. Weather Rev. 145, 3009–3023. https://doi.org/10.1175/MWR-D-17-0033.1.

Guo, N., Zhou, Y., Yang, L., 2021. Statistical analysis of Central Asian vortices and their influence on precipitation in Xinjiang. Atmos. Res. 249, 105327 https://doi.org/10.1016/j.atmosres.2020.105327.

Hawkins, H.F., Rosenthal, S.L., 1965. On the computation of stream functions from the wind field. Mon. Weather Rev. 93, 245–252. https://doi.org/10.1175/1520-0493.

Hersbach, H., Bell, B., Berrisford, P., Biavati, G., Horányi, A., Muñoz Sabater, J., Nicolas, J., Peubey, C., Radu, R., Rozum, I., Schepers, D., Simmons, A., Soci, C., Dee, D., Thépaut, J.-N., 2018. ERA5 Hourly Data on Pressure Levels from 1979 to Present. Copernicus Climate Change Service Climate Data Store. https://doi.org/10.24381/cds.bd0915c6 (Accessed on < 09-Jun-2021 >).

Hoskins, B.J., McIntyre, M.E., Robertson, A.W., 1985. On the use and significance of isentropic potential vorticity maps. Quart. J. Roy. Meteor. Soc. 111, 877–946. https://doi.org/10.1002/qj.49711147002.

Hua, S., Xu, X., Chen, B., 2020. Influence of multiscale orography on the initiation and maintenance of a precipitating convective system in North China: a case study. J. Geophys. Res. 125 https://doi.org/10.1029/2019JD031731 e2019JD031731.

Huang, R.H., Zhang, Z., Huang, G., Ren, B.H., 1998. Characteristics of the water vapor transport in east Asian monsoon region and its difference from that in south Asian monsoon region in summer. Sci. Atmos. Sin. 22, 460–469. https://doi.org/10.3878/j.issn.1006-9895.1998.04.08 (in Chinese).

Krishnamurti, T.N., 1968. A diagnostic balance model for studies of weather systems of low and high latitudes, Rossby number less than 1. Mon. Weather Rev. 96, 197–207. https://doi.org/10.1175/1520-0493.

Ma, S.P., Ran, L.K., Cao, J., 2021. Diagnosis and analysis of vertical motion during complex topographical heavy snowfall. Sci. Atmos. Sin. 45, 1127–1145. https://doi.org/10.3878/j.issn.1006-9895.2105.20206 (in Chinese).

Murakami, T., 1959. The general circulation and water-vapor balance over the Far East during the rainy season. Geophys. Mag. 29, 131–171.

Ninomiya, K., Akiyama, T., 1971. The development of the medium-scale disturbance in the Baiu front. J. Met. Soc. Japan 49, 663–672.

Ninomiya, K., Kobayashi, C., 1999. Precipitation and moisture balance of the Asian summer monsoon in 1991. Part 2: moisture transport and moisture balance. J. Meteor. Soc. Jpn. 77, 77–99. https://doi.org/10.2151/jmsj1965.77.1_77.

Parrish, D.F., Derber, J.C., 1992. The National Meteorological Center’s spectral statistical interpolation analysis system. Mon. Weather Rev. 20, 1747–1763. https://doi.org/10.1175/1520-0493(1992)120<1747:TNMCSS>2.0.CO;2.

Schiemann, R., Lüthi, D., Vidale, P.L., Schär, C., 2008. The precipitation climate of Central Asia—intercomparison of observational and numerical data sources in a remote semiarid region. Int. J. Climatol. 28, 295–314. https://doi.org/10.1002/joc.1532.

Schumacher, R.S., Johnson, R.H., 2008. Mesoscale processes contributing to extreme rainfall in a midlatitude warm-season flash flood. Mon. Weather Rev. 136, 3964–3986. https://doi.org/10.1175/2008mwr2471.1.

Shi, Y.G., Sun, Z.B., Yang, Q., 2008. Characteristics of area precipitation in Xinjiang region with its variations. J. Appl. Meteor. Sci. 19, 326–332. https://doi.org/10.3969/j.issn.1001-7313.2008.03.008. (in Chinese).

Simmonds, I., Bi, D., Hope, P., 1999. Atmospheric water vapor flux and its association with rainfall over China in summer. J. Clim. 12, 1353–1367. https://doi.org/10.1175/1520-0442(1999)012<1353:AWVFAI>2.0.CO;2.

Skamarock, W.C., Coauthors, 2008. A Description of the Advanced Research WRF Version 3. NCAR/TN-475+STR, 113pp.

Sun, B., Wang, H., 2014. Moisture sources of semiarid grassland in China using the Lagrangian particle model FLEXPART. J. Clim. 27, 2457–2474. https://doi.org/10.1175/JCLI-D-13-00517.1.

Sun, B., Wang, H., 2015. Analysis of the major atmospheric moisture sources affecting three sub-regions of East China. Int. J. Climatol. 35, 2243–2257.

Trenberth, K.E., Guiliemot, C.J., 1995. Evaluation of the global atmospheric moisture budget as seen from analyses. J. Clim. 8, 2255–2272. https://doi.org/10.1175/1520-0442(1995)008<2255:EOTGAM>2.0.CO;2.

Tripoli, G.J., Cotton, W.R., 1989. Numerical study of an observed orogenic mesoscale convective system. Part 1: simulated genesis and comparison with observations. Mon. Weather Rev. 117, 273–304. https://doi.org/10.1175/1520-0493.

Ullah, W., Wang, G., Gao, Z., Hagan, D., Bhatti, A., et al., 2020. Observed Linkage between Tibetan Plateau soil moisture and South Asian summer precipitation and the possible mechanism. J. Clim. 34, 361–377. https://doi.org/10.1175/JCLI-D-20-0347.1.

Ullah, W., Wang, G., Lou, D., Ullah, S., Bhatti, A., et al., 2021. Large-scale atmospheric circulation patterns associated with extreme monsoon precipitation in Pakistan during 1981-2018. Atmos. Res. 232, 105489 https://doi.org/10.1016/j.atmosres.2021.105489.

Wang, Q., Xue, M., Tan, Z., 2016. Convective initiation by topographically induced convergence forcing over the Dabie Mountains on 24 June 2010. Adv. Atmos. Sci. 33 (10), 1120–1136. https://doi.org/10.1007/s00376-016-6024-z.

Wang, L., Hu, X.Q., Xu, N., Chen, L., 2021. Water vapor retrievals from near-infrared channels of the advanced Medium Resolution Spectral Imager instrument onboard the Fengyun-3D satellite. Adv. Atmos. Sci. 38, 1351–1366. https://doi.org/10.1007/s00376-020-0174-8.

Xu, Q., Cao, J., Gao, S., 2011. Computing streamfunction and velocity potential in a limited domain. Part I: Theory and integral formulae. Adv. Atmos. Sci. 28, 1433–1444.

Xu, Q., Liu, S., Xue, M., 2006. Background error covariance functions for vector wind analyses using Doppler radar radial-velocity observations. Quart. J. Roy. Meteor. Soc. 132, 2887–2904. https://doi.org/10.1256/qj.05.202.

Xu, Q., Nai, K., Wei, L., 2007. An innovation method for estimating radar radial-velocity observation error and background wind error covariances. Quart. J. Roy. Meteor. Soc. 133, 407–415. https://doi.org/10.1002/qj.21.

Xu, X., Xue, M., Wang, Y., Huang, H., 2017. Mechanisms of secondary convection within a mei-yu frontal mesoscale convective system in eastern China. J. Geophys. Res.-Atmos. 122, 47–64. https://doi.org/10.1002/2016JD026017.

Xue, M., Luo, X., Zhu, K., Sun, Z., Fei, J., 2018. The controlling role of boundary layer inertial oscillations in Meiyu frontal precipitation and its diurnal cycles over China. J. Geophys. Res.-Atmos. 123, 5090–5115. https://doi.org/10.1029/2018JD028368.

Yanai, M., Esbensen, S., Chu, J.H., 1973. Determination of bulk properties of tropical cloud clusters from large-scale heat and moisture budgets. J. Atmos. Sci. 30, 611–627. https://doi.org/10.1175/1520-0469(1973)030<0611:DOBPOT>2.0.CO;2.

Yang, L.M., Zhang, Y.H., Qin, H., 2015. Some advances and problems of middle-Asia vortex. Desert Oasis Meteorol. 9, 1–8. https://doi.org/10.3969/j.issn.1002-0799.2015.05.001.

You, C., Fung, J., 2019. Characteristics of the sea-breeze circulation in the Pearl River Delta region and its dynamical diagnosis. J. Appl. Meteorol. Climatol. 58, 741–755. https://doi.org/10.1175/JAMC-D-18-0153.1.

Yuan, Z., Zhuge, X., Wang, Y., 2020. The forced secondary circulation of the Mei-yu front. Adv. Atmos. Sci. 37, 766–780. https://doi.org/10.1007/s00376-020-9177-8.

Zeng, Y., Yang, L., 2020. Triggering mechanism of an extreme rainstorm process near the Tianshan Mountains in Xinjiang, an arid region in China, based on a numerical simulation. Adv. Meteorol. https://doi.org/10.1155/2020/8828060, 8828060.

Zhang, R.H., 2001. Relations of water vapor transport from Indian monsoon with that over East Asia and the summer rainfall in China. Adv. Atmos. Sci. 18, 1005–1017. https://doi.org/10.1175/1520-0442(1999)012<1353:AWVFAI>2.0.CO;2.

Zhou, T.J., Yu, R.C., 2005. Atmospheric water vapor transport associated with typical anomalous summer rainfall patterns in China. J. Geophys. Res. 110, D08104. https://doi.org/10.1029/2004JD005413.